PHYSICAL REVIEW E **80**, 036208 (2009)

Lagrangian topology of a periodically reoriented potential flow: Symmetry, optimization, and mixing

D. R. Lester[*] and G. Metcalfe
CSIRO Materials Science and Engineering, P.O. Box 56, Highett, Victoria 3190, Australia

M. G. Trefry[†]
CSIRO Land and Water, Underwood Av., Floreat, Western Australia 6014, Australia

A. Ord[†] and B. Hobbs[†]
CSIRO Exploration and Mining, ARRC, 26 Dick Perry Av., Kensington, Western Australia 6151, Australia

M. Rudman
CSIRO Mathematical and Information Sciences, Locked Bag 33, Clayton South, Victoria 3169, Australia

(Received 28 May 2009; published 21 September 2009)

Scalar transport in closed potential flows is investigated for the specific case of a periodically reoriented dipole flow. Despite the irrotational nature of the flow, the periodic reorientations effectively create heteroclinic and/or homoclinic points arising from the joining of stable and unstable manifolds. For scalar advection, Lagrangian chaos can be achieved with breakdown of the regular Hamiltonian structure, which is governed by symmetry conditions imposed by the dipole flow. Instability envelopes associated with period-doubling bifurcations of fixed points govern which regions of the flow control parameter space admit global chaos. These regions are further refined via calculation of Lyapunov exponents. These results suggest significant scalar transport enhancement is possible within potential flows, given appropriate programming of stirring protocols.

DOI: 10.1103/PhysRevE.80.036208 PACS number(s): 05.45.−a, 47.52.+j, 47.51.+a

I. INTRODUCTION

Potential flows capture the gross mechanics of a wide range of applications involving flow within porous media including, e.g., leaching of minerals or contaminants from aquifer formations, oil recovery in shale beds, carbon sequestration in calcium carbonate and recovery of geothermal heat. These processes are unified by the process-limiting transport of some entity such as heat, chemical reagent, or pollutant; however research into transport enhancement in such flows has been limited and in the geophysical literature there is controversy over whether mixing in porous media flows is possible [1]. A well-known mechanism to achieve mixing within low Reynolds number flows is via chaotic advection [2], whereby flows which although simple in the Eulerian sense exhibit chaotic dynamics in the Lagrangian frame: from a kinematic perspective the advection equation describing motion of a passive tracer

$$\dot{\mathbf{x}} = \mathbf{v}(\mathbf{x},t) \tag{1}$$

with $\nabla \cdot \mathbf{v} = 0$, represents a dynamical system rich enough to generate chaotic particle paths. In Eq. (1), $\mathbf{v}$ is the fluid velocity field, t time, and $\mathbf{x}$ physical space, corresponding to the state space of the dynamical system. Hence chaotic dynamics (and associated manifolds) within the state space can be directly observed as evolving mixing patterns in dye trace experiments. As such the transport dynamics of such flows can be inferred directly from the Lagrangian topology of Eq. (1) such that “good mixing” or rapid transport corresponds to global chaos throughout the flow domain, ensuring complete mixing to small length scales within finite time. Although these principles have been applied widely to low Reynolds number flows in general, the study of chaotic advection within potential flows is limited [3,4]. A necessary requirement for chaotic dynamics is the existence of heteroclinic and/or homoclinic points arising from the joining of stable and unstable manifolds [5]. Due to the irrotational nature of potential flows, heteroclinic or homoclinic connections cannot occur in steady two-dimensional (2D) or three-dimensional (3D) potential flows, in contrast to steady 3D Stokes flows which may admit Lagrangian chaos. However, heteroclinic and/or homoclinic connections can be created in *transient* potential flows via the transient crossing of streamlines. This phenomenon has been investigated in only a handful of applications [4,6,7] and little is known about the topology of such systems.

For a given flow device, an open question for both potential and Stokes flows is what boundary motions and/or flow forcings generate global Lagrangian chaos and optimal scalar transport? To date, no investigation of transport optimization via Lagrangian chaos has been performed for potential flows and while it has been shown that chaotic advection can be achieved for such flows, the level of scalar transport enhancement for optimized potential flows has not been established. Parameterization of the transient flow field $\mathbf{v}(\mathbf{x},t)$ in terms of a set of “base flows” generates a formal mathematical basis for the optimization of scalar transport, and Hamiltonian dynamics provides a convenient framework for analysis. As the breakdown of integrable states to chaos and the

---

[*] daniel.lester@csiro.au

[†] Also at University of Western Australia, School of Earth and Environment, 35 Stirling Highway Crawley, WA 6009.

Lagrangian topology itself is constrained by symmetries in the domain geometry and boundary conditions, analysis of these symmetries generates significant insight into the mechanisms governing scalar transport. In this paper we apply such analyses along with standard tools of dynamical systems (Poincaré sections, Lyapunov exponents) to study and optimize scalar transport in a model potential flow. These results quantify the scope for transport enhancement in potential flows in general and provide insight into the mechanisms governing Lagrangian dynamics in such systems.

II. PROBLEM DEFINITION

Rotated potential mixing flow and governing parameters

As we are interested in the fundamentals of transport enhancement, study of particularly simple potential flows may generate greater insight while simplifying analysis. Following Metcalfe *et al.* [8], the fundamentals of transport in porous media are well represented by a 2D dipole flow, as many porous media flows can be well approximated by superposition of a number of dipole flows. The 2D dipole flow is described by the complex potential

$$F(z) = \log\left(\frac{z+1}{z-1}\right), \tag{2}$$

corresponding to source and sinks along the real line at ±1 [9]. This potential is mapped to a disk by the Schwarz-Christoffel transform

$$z = i\frac{w+1}{w-1}, \tag{3}$$

where the upper half of the complex plane is mapped to the domain $\mathcal{D}:\{r,\theta\}=[0,1]\times[-\pi,\pi]$ in cylindrical coordinates $\{r,\theta\}$, and the lower half is mapped outside $\mathcal{D}$, divided by a separating streamline along the domain boundary $\partial\mathcal{D}:r=1$. The source $\mathbf{x}^+$ and sink $\mathbf{x}^-$ occur on the disk boundary at $\{r,\theta\}=(1,\pi/2)$ and $(1,-\pi/2)$, respectively, as depicted in Fig. 1(a), and the velocity potential φ and streamfunction ψ respectively are given by the real and imaginary parts of $F(w)$

$$\varphi = \mathrm{Re}[F(w)] = \frac{1}{2}\log\left(\frac{r^2-2r\sin\theta+1}{r^2+2r\sin\theta+1}\right), \tag{4}$$

$$\psi = \mathrm{Im}[F(w)] = \arctan\left(\frac{2r\cos\theta}{1-r^2}\right). \tag{5}$$

What we will call the flow velocity field is $\hat{\mathbf{v}}=\nabla\varphi=\nabla\times\psi\hat{\mathbf{e}}_z$, where $\hat{\mathbf{e}}_z$ is the unit vector in the z direction. To create heteroclinic or homoclinic points and hence Lagrangian chaos, a necessary condition is the transient crossing of streamlines. The simplest stirring protocol to achieve such behavior is to let $\hat{\mathbf{v}}$ operate for a fixed time τ, after which the dipole positions are instantaneously reoriented about the origin through angle Θ, after which the dipole flow again operates for time τ and so on. This flow is named the RPM flow, the transient velocity field of which can be approximated as

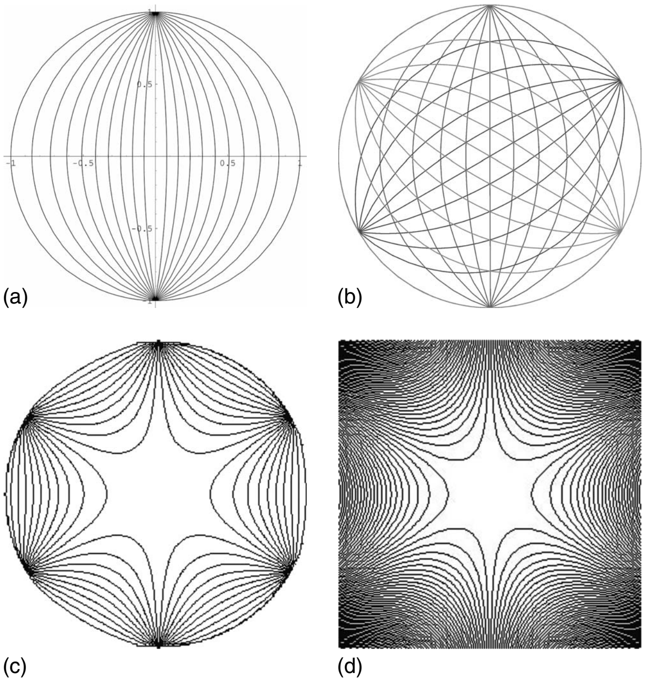

FIG. 1. (a) Contours of dipole flow streamfunction with inlet (outlet) $\mathbf{x}^+(\mathbf{x}^-)$ at $r=1$, $\theta=\pi/2(\theta=-\pi/2)$, (b) superimposed streamlines for reoriented flow with $\Theta=2\pi/3$, (c) corresponding Hamiltonian, and (d) detail of stagnation point at the origin.

$$\mathbf{v}(\mathbf{x},t;\tau,\Theta) \approx \hat{\mathbf{v}}\left(r,\theta+\left\lfloor\frac{t}{\tau}\right\rfloor\Theta\right), \tag{6}$$

where $\lfloor x \rfloor$ denotes the integer part of x. Elsewhere, we have experimentally realized the RPM flow [10,11] for studies involving coupled transport, deformation and reaction and found dye advection visualizations to agree well with theory. If the viscous time scale R_0^2/κ is small (where R_0 and κ, respectively, are the disk radius and fluid kinematic viscosity) with respect to the reorientation frequency $R_0/\tau v_0$ (where v_0 is fluid velocity at the origin), then transient effects associated with dipole reorientations as quantified by the Strouhal number $St=Re/\tau$ may be ignored. We assume the Reynolds number $Re=v_0R/\kappa$ is negligible, and so the approximation Eq. (6) is exact for finite τ. Introducing the nondimensional variables $r'=r/R_0$, $\mathbf{v}'=2\mathbf{v}/v_0$, and $t'=tv_0/R_0$ (and henceforth dropping the primes), the RPM is fully described by the control parameters τ and Θ. These parameters define the stirring protocol and hence dictate the Lagrangian topology and transport dynamics of the RPM flow.

Superposed reoriented streamlines for $\Theta=2\pi/3$ are depicted in . 1(b). Clearly for values of Θ commensurate with π, this temporal flow is periodic with period $T=j\tau$, where $\Theta=k/j2\pi$ for some integers j and k, however for irrational Θ/π, the aperiodic flow only represents a conceptual difference. Study of the global structure of transport in the RPM flow corresponds to analysis of the Lagrangian dynamics of Eq. (1) over the parameter space of the flow: $\mathcal{Q}:\{\tau,\Theta\}=[0,\infty)\times[-\pi,\pi]$.

Two fundamentally distinct modes of operation are possible for this flow, characterized by whether the domain $\mathcal{D}$ is open or closed. For the open problem, the source $\mathbf{x}^{+}$ and sink $\mathbf{x}^{-}$ represent inflow and outflow boundaries, whereas for the closed problem $\mathbf{x}^{+}$, $\mathbf{x}^{-}$ are symmetry boundaries, i.e., any material leaving $\mathbf{x}^{-}$ is instantaneously reinjected at $\mathbf{x}^{+}$ on the same streamline to preserve continuity. As illustrated for other potential flows [4], different reinjection protocols (delayed, reflected, stochastic) generate different transport properties for the RPM flow. The open and closed modes of operation have fundamentally different characteristics, both of which shall be considered in this paper.

III. FLOW SYMMETRIES

Transport properties of the RPM flow are governed by the topology of the Lagrangian dynamics. This topology is "programmed" by regular reorientation of the base flow $\hat{\mathbf{v}}$, and so symmetries in this base flow play an important role in the ordering of coherent structures and breakdown of the integrable state. As the Hamiltonian for an incompressible fluid corresponds to the streamfunction, the time-averaged Hamiltonian H for the RPM flow is

$$H=\begin{cases}\dfrac{1}{j}\displaystyle\sum_{n=0}^{j-1}\psi(r,\theta-n\Theta) & \text{for}\;\;\Theta=2\pi\dfrac{k}{j},\\[2ex] \displaystyle\int_{-\pi}^{\pi}\psi(r,\theta)d\theta & \text{for irrational},\dfrac{\Theta}{\pi},\end{cases}\qquad(7)$$

which is steady in the limit $\tau\rightarrow 0$. As the streamfunction ψ for the dipole flow has the reflection-reversal $\psi(r,\theta)=-\psi(r,\theta+\pi)$, then the Hamiltonian H above is identically zero in all cases in Eq. (7) except for rational Θ where the denominator j is odd. At the origin $r=0$, there exists an elliptic point of measure zero, as depicted in . 1(d). For all cases in the limit $\tau\rightarrow 0$, this system is integrable and coherent structures in the Poincaré section correspond to isopleths of H, as depicted in . 1(c). With increasing τ, this integrable state breaks down in an eventual route to chaos and the symmetries inherent to $\hat{\mathbf{v}}$ have consequences for this breakdown.

If the solution to the conservative system Eq. (1) with the velocity field described by Eq. (6) describing particle transport represents a continuous flow (in the dynamical systems sense) $\hat{\mathbf{\Upsilon}}_t$, then

$$\mathbf{x}(t)=\hat{\mathbf{\Upsilon}}_t[\mathbf{x}(0)],\qquad(8)$$

and this flow can be reduced to a map that operates in the dipole frame of reference

$$\mathbf{\Upsilon}=\mathbf{R}^{-1}\int_0^{\tau}\hat{\mathbf{\Upsilon}}_t dt,\qquad(9)$$

where $\mathbf{R}$ is the rotation operator

$$\mathbf{R}:\theta\rightarrow\theta+\Theta.\qquad(10)$$

As the Lagrangian topology is invariant under $\mathbf{R}$, then the dynamics of the stroboscopic map $\mathbf{\Upsilon}$ in the dipole frame is equivalent to that of the continuous map $\hat{\mathbf{\Upsilon}}_t$ in the laboratory frame. The advantage of such an approach is that the system Eq. (1) in the dipole frame is τ periodic, simplifying analysis of $\mathbf{\Upsilon}$, especially for values of $\mathbf{\Theta}$ incommensurate with π. If $\mathbf{x}_n$ represents the location of a fluid particle in the dipole frame at time $t=n\tau$, then the map

$$\mathbf{x}_{n+1}=\mathbf{\Upsilon}(\mathbf{x}_n),\qquad(11)$$

describes evolution of the dynamical system Eq. (1) for integer values of τ. If the stroboscopic map associated with the base flow $\hat{\mathbf{v}}$ over time τ is denoted $\mathbf{\Upsilon}_0$, then from Eq. (9) $\mathbf{\Upsilon}=\mathbf{R}^{-1}\mathbf{\Upsilon}_0$.

From the domain geometry and boundary conditions [. 1(a)], the base flow $\hat{\mathbf{v}}$ contains two symmetries: a reflection symmetry along the y axis, and a reflection-reversal symmetry along the x axis, formalized as

$$\mathbf{\Upsilon}_0=\mathbf{S}_0\mathbf{\Upsilon}_0\mathbf{S}_0,\quad \mathbf{S}_0:\theta\rightarrow\pi-\theta,\qquad(12)$$

$$\mathbf{\Upsilon}_0=\mathbf{S}_1\mathbf{\Upsilon}_0^{-1}\mathbf{S}_1,\quad \mathbf{S}_1:\theta\rightarrow-\theta,\qquad(13)$$

Substitution of Eq. (12) into Eq. (9) yields

$$\mathbf{\Upsilon}=\mathbf{R}^{-1}\mathbf{S}_0\mathbf{\Upsilon}_0\mathbf{S}_0=\mathbf{R}^{-1}\mathbf{S}_0\mathbf{R}\mathbf{\Upsilon}\mathbf{S}_0,\qquad(14)$$

and using $\mathbf{R}=\mathbf{S}_0\mathbf{R}^{-1}\mathbf{S}_0$ and $\mathbf{S}_0^2=\mathbf{I}$, then

$$\mathbf{S}_0\mathbf{\Upsilon}\mathbf{S}_0=\mathbf{R}^2\mathbf{\Upsilon}=\mathbf{P}(\Upsilon),\qquad(15)$$

where $\mathbf{P}$ is the operator which maps $\mathbf{\Theta}\rightarrow-\mathbf{\Theta}$. Therefore, the reflection symmetry of the base flow along the y axis yields a reflection symmetry in the Lagrangian topology between positive and negative offsets $\mathbf{\Theta}$. Due to this degeneracy, the flow parameter space can be reduced to $\mathcal{Q}:\{\tau,\Theta\}=[0,\infty)\times[0,\pi]$ without loss of topological information. Substitution of the symmetry

$$\mathbf{S}_2=\mathbf{R}^{-1}\mathbf{S}_1\Leftrightarrow\mathbf{S}_1=\mathbf{R}\mathbf{S}_2,\quad \mathbf{S}_2:\theta\rightarrow\theta-\Theta,\qquad(16)$$

into Eq. (13) and Eq. (9) yields

$$\mathbf{\Upsilon}=\mathbf{R}^{-1}\mathbf{S}_1\mathbf{\Upsilon}_0^{-1}\mathbf{S}_1=\mathbf{S}_2\mathbf{\Upsilon}^{-1}\mathbf{S}_2,\qquad(17)$$

and so $\mathbf{\Upsilon}$ also satisfies the reflection-reversal symmetry $\mathbf{S}_2$, further constraining coherent structures in the Lagrangian topology to evolve symmetrically about $\theta=-\Theta/2$.

The particularly simple form of the dipole base flow facilitates a semianalytic expression for the RPM flow map $\mathbf{\Upsilon}$, generating significant analytic and computational benefits for the study of transport. To simplify the map $\mathbf{\Upsilon}$ parameterized by $\tau,\mathbf{\Theta}$, the transport problem for the dipole potential flow is solved first. As shall become apparent, it is convenient to introduce the modified radial coordinates

$$r'=\begin{cases}r & |\theta|<\dfrac{\pi}{2}\\[2ex] -r & |\theta|\geq\dfrac{\pi}{2}\end{cases},\qquad(18)$$

$$\theta'+\frac{\pi}{2}=\theta+\frac{\pi}{2}\bmod\pi,\qquad(19)$$

such that the circular domain $\mathcal{D}$ is now described as $\{r',\theta'\}=[-1,1]\times[-\frac{\pi}{2},\frac{\pi}{2}]$. Note that Eq. (19) represents a

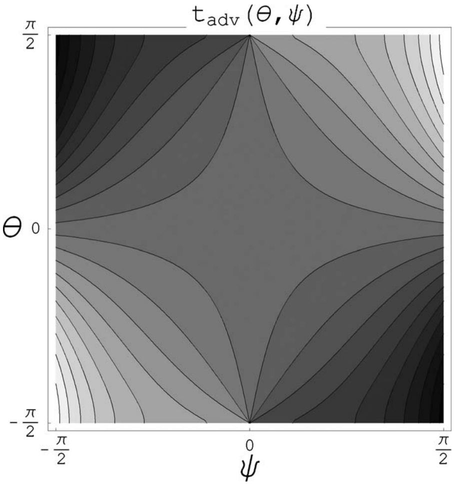

FIG. 2. Contour plot of the advection time $t_{\rm adv}$, ranging from −1 (white) to +1 (black).

change in the coordinate limits only; a line of constant θ' now bisects the domain $\mathcal{D}$ while passing through the origin. For simplicity the primes are henceforth dropped from r', θ'.

As fluid particles travel along streamlines of constant ψ during advection, a natural coordinate system for the problem is in terms of $\{\theta,\psi\}$. If s denotes the distance along a given streamline, then the differential element ds is given by $ds^2=dr^2+r^2d\theta^2$, where r and θ are related via Eq. (5) for fixed ψ. The rate of change in stream distance defines the streamline velocity, equivalent to the velocity norm, and has the simple form upon elimination of θ

$$\frac{ds}{dt} \equiv |\mathbf{v}| = \frac{2\cos\psi}{1-r^2}. \tag{20}$$

Eliminating r, differential time dt may be expressed as

$$dt = \frac{\sqrt{\left(\frac{\partial r}{\partial\theta}\right)^2 + r^2}}{|\mathbf{v}|}d\theta = \frac{(\sqrt{1+b^2}-b)-(\sqrt{1+b^2}-b)^3}{2\sqrt{1+b^2}}d\theta, \tag{21}$$

where $b=\cos\theta\cot\psi$. Integration of Eq. (21) yields the advection time $t_{\rm adv}$ along a streamline

$$t_{\rm adv}(\theta,\psi) = \frac{|\psi|}{\psi}\csc^2\psi\left(\cot\psi\arctan\left[\frac{\sin\theta\cot\psi}{\sqrt{1+\cos^2\theta\cot^2\psi}}\right] + \sin\theta\sqrt{1+\cos^2\theta\cot^2\psi} - |\cot\psi|(\theta+\cos\theta\sin\theta)\right) \tag{22}$$

Symmetries of the flow are preserved; $t_{\rm adv}$ is odd with respect to both θ and ψ as depicted in Fig. 2. As $t_{\rm adv}(0,\psi)=0$, $t_{\rm adv}(\theta_1,\psi)$ represents the time for a particle to be advected from $\theta=\theta_1$ to $\theta=0$ along streamline ψ, as per Fig. 3(a). Hence negative advection times arise for particles downstream of the centerline $\theta=0$. The residence time $T_{\rm res}$ of a fluid particle injected at $\mathbf{x}^+$ on streamline ψ to exit at $\mathbf{x}^-$ is

$$T_{\rm res}(\psi) \equiv \frac{|\psi|}{\psi}\left[t_{\rm adv}\left(\frac{\pi}{2},\psi\right) - t_{\rm adv}\left(-\frac{\pi}{2},\psi\right)\right],$$

$$=\csc^2\psi(2-\cot\psi)\left(\frac{\pi}{2}-\psi\right), \tag{23}$$

which is plotted in Fig. 3(b), ranging from $T_{\rm res}(0)=\frac{2}{3}$ for the centerline trajectory to $T_{\rm res}(\pm\frac{\pi}{2})=2$ for the separation streamlines.

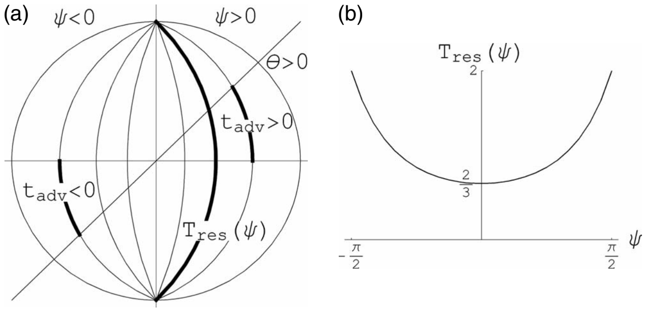

FIG. 3. (a) Schematic depicting the advection $t_{\rm adv}$ and residence $T_{\rm res}$ times, (b) plot of $T_{\rm res}$.

For the closed problem, a fluid particle at initial position θ_1 advected for time τ is then positioned at θ_2 such that

$$t_{\rm adv}(\theta_2,\psi) + \frac{T_{\rm res}}{2} = t_{\rm adv}(\theta_1,\psi) + \frac{T_{\rm res}}{2} + \tau \bmod T_{\rm res}, \tag{24}$$

however Eq. (22) cannot be solved analytically for θ in terms of $t_{\rm adv}$ and ψ. Inversion can be performed numerically by calculation of Eq. (22) to high resolution over $\{\theta,\psi\}=[-\frac{\pi}{2},\frac{\pi}{2}]\times[-\frac{\pi}{2},\frac{\pi}{2}]$ to form the interpolation function $\theta_{\rm interp}(t_{\rm adv},\psi)$, so defining the advection map $\mathbf{Y}_0$ for $t=\tau$

$$\mathbf{Y}_0:\{\theta_1,\psi\} \to \{\theta_2,\psi\}. \tag{25}$$

Likewise the rotational map $\mathbf{R}$ is given by

$$\mathbf{R}:\{\theta,\psi\} \to \left\{\theta+\Theta, \arctan\left(\frac{\cos(\theta+\Theta)}{\cos\theta}\tan\psi\right)\right\}, \tag{26}$$

and so the composite map $\mathbf{Y}=\mathbf{R}^{-1}\mathbf{Y}_0$ fully describes advection of fluid particles under the flow $\dot{\mathbf{x}}=\mathbf{v}(\mathbf{x},t)$ for integer multiples of time τ in the dipole frame of reference. Expression of the dynamics of Eq. (1) in terms of the map $\mathbf{Y}$ facilitates both rapid computation of mixing simulations and Poincaré sections, and furthermore permits stability analysis in the neighborhood of fixed points of the system.

IV. FIXED POINTS

The stability of period p points of the stroboscopic map $\mathbf{Y}^p(\mathbf{x}_0)=\mathbf{x}_0$ derived above directly controls the local transport dynamics of the flow. Nondegenerate periodic points of Hamiltonian systems are either elliptic or hyperbolic: elliptic points are locally stable and generate nonmixing islands. Conversely, hyperbolic points are locally unstable and possess stable and unstable manifolds, which may intersect to form heteroclinic or homoclinic connections, a signature of

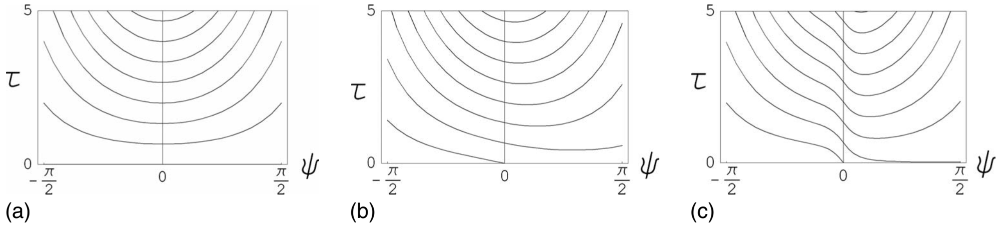

FIG. 4. Fixed point contours according to Eq. (27) for (a) $\Theta=0$, (b) $\Theta=\frac{\pi}{2}$, and (c) $\Theta=\frac{9\pi}{10}$.

chaos. The bifurcation of elliptic periodic points to hyperbolic represents a necessary but not sufficient condition for complete global mixing. The dominant periodic points of the map $\mathbf{\Upsilon}$ are generally the fixed points, i.e., $p=1$. As period-1 fixed points must reside on the same streamline for all times, ψ must be invariant under mapping via $\mathbf{R}$ for these points. From Eq. (26) for ψ to remain constant $\theta=-\Theta/2$; i.e., all fixed points lie on the axis of symmetry $\theta=-\Theta/2$, recovering the symmetry result Eq. (17).

From Eq. (24), period-1 fixed points satisfy the relation

$$\tau = nT_{\mathrm{res}}(\psi) - 2t_{\mathrm{adv}}\left(\frac{\Theta}{2},\psi\right) \tag{27}$$

for $n=0,1,2..$, where n represents the number of times a point is reinjected from the sink $\mathbf{x}^-$ to the source $\mathbf{x}^+$. The open system corresponds to the restriction $n=0$. Figures 4(a)–4(c) depict the loci of Eq. (27) for all n at various values of Θ. For a given τ, fixed points occur at values of ψ given by the intersection of these lines with the horizontal line of constant τ. As $\partial t_{\mathrm{adv}}/\partial\psi > 0\,\forall\{\theta,\psi\}\in[0,\pi/2]\times[-\pi/2,\pi/2]$, and $\operatorname{sgn} dT_{\mathrm{ref}}/d\psi = \operatorname{sgn}\psi\,\forall\,\psi\in[-\pi/2,\pi/2]$, the right hand side of Eq. (27) is monotonic increasing with $|\psi|$ for $\psi<0$, whereas turning points can occur [as per Figs. 4(b) and 4(c)] for $\psi>0$.

Consequently, for both open and closed systems, the fixed point which occurs at the origin in $\mathcal{D}$ for $\tau=0$ and all Θ moves along the $\theta=-\Theta/2$ axis of symmetry in the negative ψ direction. This fixed point reaches the separating streamline $\psi=-\pi/2$ at $\tau=2t_{\mathrm{adv}}(-\Theta/2,-\pi/2)$, leaving the system at greater values of τ. Hence for the open system there is at most only one fixed point of the flow, which occurs for $\tau \le 2t_{\mathrm{adv}}(-\Theta/2,-\pi/2)$, and so from (22) the fixed point existence boundary for the open flow evaluates to the line

$$\tau = \sin(\Theta/2). \tag{28}$$

For closed systems ($n>0$), fixed points also occur at the origin for $\tau=2n/3$, $n=1,2,\ldots$, and reach the $\psi=-\pi/2$ separating streamline at $\tau=2n-2\Theta/\pi$ before leaving the system at greater values of τ. As fixed points occur at the origin for $\tau=2n/3$, the number of fixed points entering the $\psi<0$ domain is $1+\lfloor 3\tau/2\rfloor$, and the number leaving is $\lceil \tau/2-\Theta/\pi\rceil$, and so the number of fixed points $n_{\mathrm{pts},\psi<0}$ in $\psi<0$ is

$$n_{\mathrm{pts},\psi<0} = 1 + \lfloor 3\tau/2\rfloor - \lceil \tau/2 - \Theta/\pi\rceil. \tag{29}$$

Due to the symmetry of the dipole flow along $\psi=0$, the number of period-1 fixed points differs between $\psi>0$ and $\psi<0$ by at most 1, hence the total number n_{pts} of fixed points in $\mathcal{D}$ for the closed flow is

$$n_{\mathrm{pts}} \approx 2 + \lfloor 3\tau\rfloor - \lceil \tau - 2\Theta/\pi\rceil, \tag{30}$$

and the number of fixed points in $\psi<0$ increases approximately as 2τ for all Θ. Exceptions do occur due to the rounding operators in Eq. (29); for $\Theta<\pi/3$ and $2\Theta/\pi<\tau<2-2\Theta/\pi$, no period-1 fixed points occur at all. However, in general the number of period-1 fixed points within the closed system increases rapidly with τ, and so the influence that the stability of these points has upon the mixing dynamics is profound.

V. STABILITY ANALYSIS

A. Stability of $n=0$ fixed points

From Eq. (7), fixed points in $\mathcal{D}$ begin at low $\tau=0$ as regular elliptic points near the origin, and the bifurcation of these fixed points to hyperbolic is necessary for complete mixing within $\mathcal{D}$. The stability properties of fixed points are governed by the nature of the mapping of a material element back onto itself in the neighborhood local to the fixed point, so a change in intersection type corresponds to a change in stability [12]. Figure 5 illustrates the bifurcation of a period-1 elliptic point on the $\theta=-\Theta/2$ axis of symmetry, depicting a material line (black) and its period-1 iterate (gray) under $\mathbf{\Upsilon}$. Prior to bifurcation at $\tau=\tau_l$ [see Fig. 5(a)], the intersection is a simple crossing at the period-1 elliptic point, and the material line has positive gradient with respect to its iterate. With increasing τ [Fig. 5(b)], the iterated material line now possesses an inflection point, yielding a negative gradient at the intersection with its iterate. This topological change corresponds directly to bifurcation of the period-1 point to hyperbolicity and two period-2 points are born on either side of this point at the intersections. As these points are elliptic their intersections possess the same relative topology as the original elliptic point. With increasing τ, these points bifurcate again in a period-doubling cascade to eventual accumulation and chaos. Transitions as such are expected as the mean stretch between reorientations of any flow increases with τ.

However, reverse period-doubling cascades are also observed in some regions, where the system converges from chaos to stability with increasing τ. This is evident in s. 6 and 8(d), where the nonreinjected contour [$n=0$ in Eq. (27)] undergoes reverse period doubling back to a stable elliptic point with increasing τ. As such, there exists an envelope of *instability* for the nonreinjected fixed points whereby the fixed point is unstable over the region $\tau_l<\tau<\tau_u$. This change is illustrated in Fig. 6, which shows the reverse cascade with increasing τ over the windows (a)–(c), and the

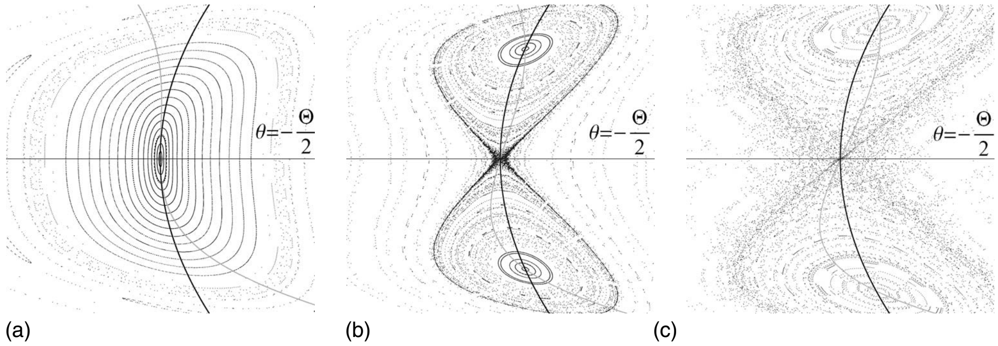

FIG. 5. Period doubling bifurcation of period-1 point at $\Theta=\frac{4\pi}{5}$ at (a) $\tau=\tau_l-\frac{1}{100}$, (b) $\tau=\tau_l$, (c) $\tau=\tau_l+\frac{1}{100}$.

instability envelope is depicted in Fig. 7, the onset of which occurs at $\Theta=\Theta_{\text{crit}}\approx 0.65\pi$. The upper solid line in Fig. 7 depicts the upper limit of τ for which nonreinjected fixed points exist within the system.

As sensitivity to initial conditions is one informal indicator of chaos, calculation of Lyapunov exponents within the instability envelope quantifies expansion of manifolds within the chaotic sea. This stretch rate is quantified by the eigenvalues of the deformation tensor

$$\mathbf{F}=\frac{\partial \mathbf{Y}}{\partial \mathbf{x}} \Leftrightarrow \frac{d\mathbf{F}}{dt}=(\nabla \mathbf{v})\cdot \mathbf{F}, \quad \mathbf{F}(0)=\mathbf{I}, \tag{31}$$

over one period of the flow. As the flow is incompressible, area is preserved and $\det(\mathbf{F})=1$, leading to reciprocal eigenvalue pairs $\{\Lambda,\Lambda^{-1}\}$. For elliptic points, $\{\Lambda,\Lambda^{-1}\}$ represent a complex conjugate pair with $|\Lambda|=1$, whereas for hyperbolic points λ is real, with $|\Lambda|>1$ quantifying the rate of expansion around the fixed point over one period. The Lyapunov exponent for this flow is simply

$$\lambda=\frac{1}{\tau}\log|\Lambda|, \tag{32}$$

and contours of λ for different values of Θ and τ within the instability envelope are depicted in Fig. 7; the highest stretch rates occur toward the limit $\Theta\to\pi$, but at $\Theta=\pi$ the system collapses to a completely integrable state. The stretching distributions in Fig. 7 suggest that optimal scalar transport occurs in the limit $\Theta\to\pi$ for values of τ around $\tau\approx 1$; however, large islands occur in this region of parameter space. The islands are associated with elliptic fixed points which pass through the periodic source/sink at $\mathbf{x}^+,\mathbf{x}^-$, and so the stability of these points must be considered.

B. Stability of $n>0$ fixed points

From Fig. 4, the origin and fate of period-1 fixed points within the system for $n>0$ can be summarized as follows. At some critical value of τ unique to each n, a new fixed point of marginal stability is born at ψ_{crit}, given by the turning points of Eq. (27) with respect to ψ. With increasing τ, two fixed points emerge which respectively move with increasing and decreasing ψ, and leave the domain at $\tau=2[n-\sin(\Theta/2)]$, $\tau=2[n+\sin(\Theta/2)]$, respectively. The stability of these points is depicted in Figs. 8(a)–8(d), where the black and gray lines correspond to elliptic and hyperbolic points, respectively. The left-moving (i.e., decreasing ψ with increasing τ) points are elliptic, but can undergo period-doubling bifurcations as depicted by the solid circles in Fig. 8. Similar to the nonreinjected points, with increasing τ these hyperbolic points can also undergo a further reverse period-doubling cascade back to elliptic type, and so the instability envelope also extends to the reinjected fixed points. The width of this instability envelope increases with Θ as per the non-reinjected points (Fig. 7), and also with increasing n or τ.

Conversely, the open circles in Figs. 8(a)–8(d) do not depict a bifurcation per se, but rather the birth of a marginally stable fixed point at the turning point of Eq. (27), denoted ψ_{crit}. At higher values of τ, fixed points at $\psi>\psi_{\text{crit}}$ are universally hyperbolic, whereas points at which $0<\psi<\psi_{\text{crit}}$ are elliptic. Due to the nature of the turning point, this region of stability universally decreases with increasing τ and in-

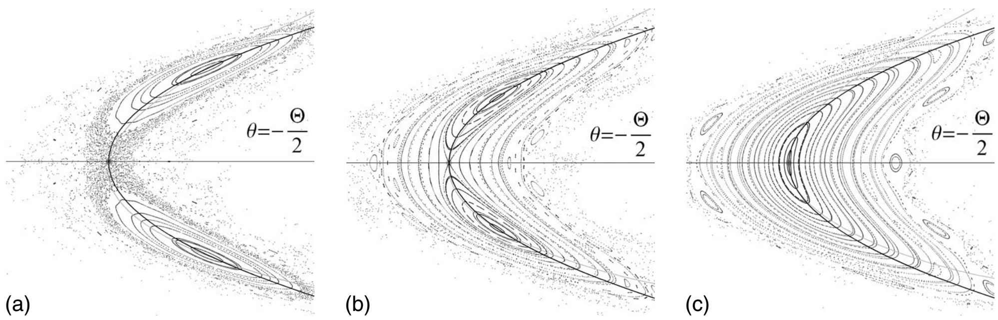

FIG. 6. Reverse period doubling cascade of period-1 point at (a) $\tau=\tau_u-\frac{1}{500}$, (b) $\tau=\tau_u$, (c) $\tau=\tau_u+\frac{1}{500}$ across the instability envelope.

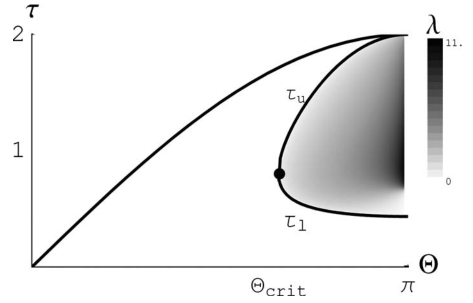

FIG. 7. Bifurcation envelope and Lyapunov exponent λ of the nonreinjected period-1 elliptic point for Θ.

creases with increasing Θ, in dischord with the period-doubling bifurcations above.

Hence the minimum conditions for globally chaotic Lagrangian dynamics within the RPM flow over the parameter space $\mathcal{Q}$ can be recast as the existence of horizontal lines of fixed τ in Fig. 8 at a given Θ which only intersect gray lines depicting hyperbolic fixed points. As $t_{\text{adv}}(\theta,0)=0$, for all Θ there always exists a region of stability around $\psi=0$ for

$$\tau=\frac{2n}{3},\quad n=0,1,2,\ldots, \tag{33}$$

which in the limits $\Theta\downarrow 0$, $\Theta\uparrow\pi$, lie on the $\psi<0$ and $\psi>0$ sides, respectively. For intermediate values of Θ, this region is two sided and monotonic decreasing in ψ-space with increasing τ. In τ space this region is more strongly monotonic decreasing as the gradient of Eq. (27) at $\psi=0$ also limits to zero with increasing τ. As such there exist bands of stability in τ for any value of Θ located around $\tau=2n/3$ which become narrower with increasing τ, and furthermore the area of the integrable region around elliptic points also decreases. These stability bands are of minimal thickness for intermediate values of Θ and coalesce into continua in the limits $\Theta\downarrow 0$, $\Theta\uparrow\pi$.

Also if a reverse period-doubling cascade exists, a region of stability can occur from $\psi=-\pi/2$ to some intermediate value in $(-\pi/2,0)$. This region of stability is also monotonic decreasing in ψ space with increasing τ, however as the gradient of Eq. (27) at $\psi=-\pi/2$ increases with increasing τ, the width of this region is approximately constant in τ space. The stability bands are of minimal thickness in the limit $\Theta\to\pi$, and coalesce into a continuum in the limit $\Theta\to 0$.

Plots of these stability bands associated with the presence of elliptic points prior to bifurcation to hyperbolic type and after reverse bifurcation back to elliptic type are shown in Figs. 9(a) and 9(b) respectively, where each band corresponds to a particular value of n in Eq. (27). The "steps" in the low-Θ region of the Fig. 9(a) correspond to regions where the elliptic points do not bifurcate at all. In Fig. 9(b), no unstable regions in $\mathcal{Q}$ occur for $\Theta<\pi/2$, although there do exist Poincaré sections in $\mathcal{Q}$ which are globally ergodic at high τ. Increased resolution of these Poincaré sections reveal regular islands and Kolmogorov-Arnold-Moser tori which appear to approach measure zero in the limit $\tau\to\infty$. As globally ergodic flows can only occur within the white regions, the area represented by the intersection of the white regions in Fig. 9 serves as a basic map for the necessary conditions for transport optimization; however, it does not account for the stability of higher-order points above period 1.

If the stability of higher-order points is taken into consideration and global ergodicity is assured, then the rate of stretching of unstable manifolds in the flow must also be

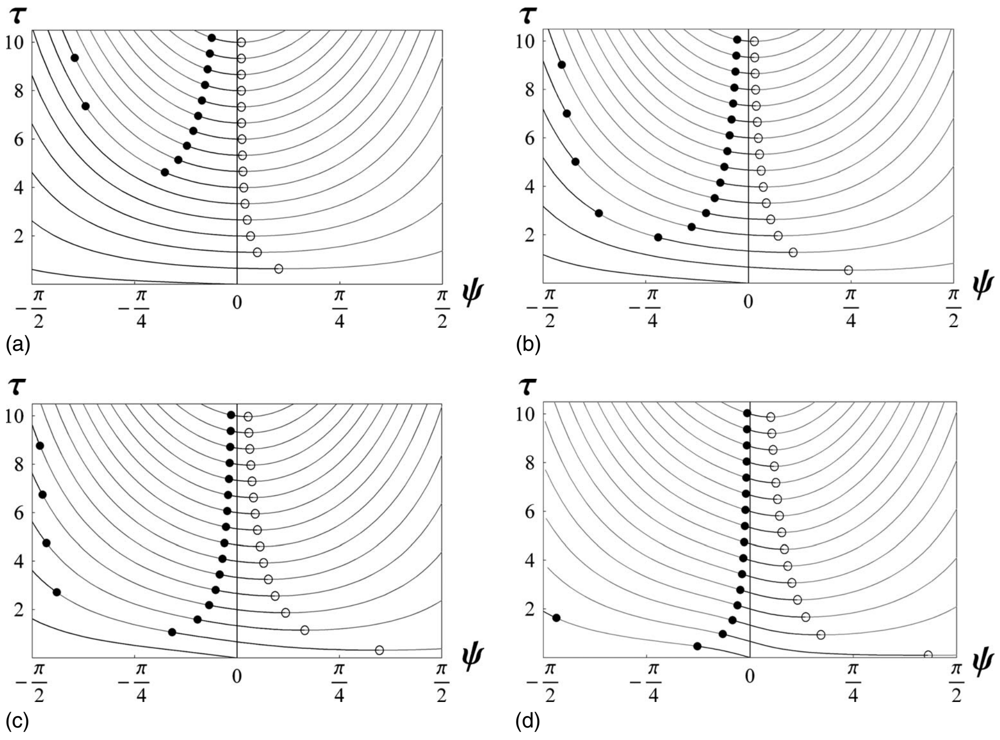

FIG. 8. Bifurcation and stability diagrams for RPM flow at (a) $\Theta=\pi/5$, (b) $\Theta=2\pi/5$, (c) $\Theta=3\pi/5$, and (d) $\Theta=4\pi/5$.

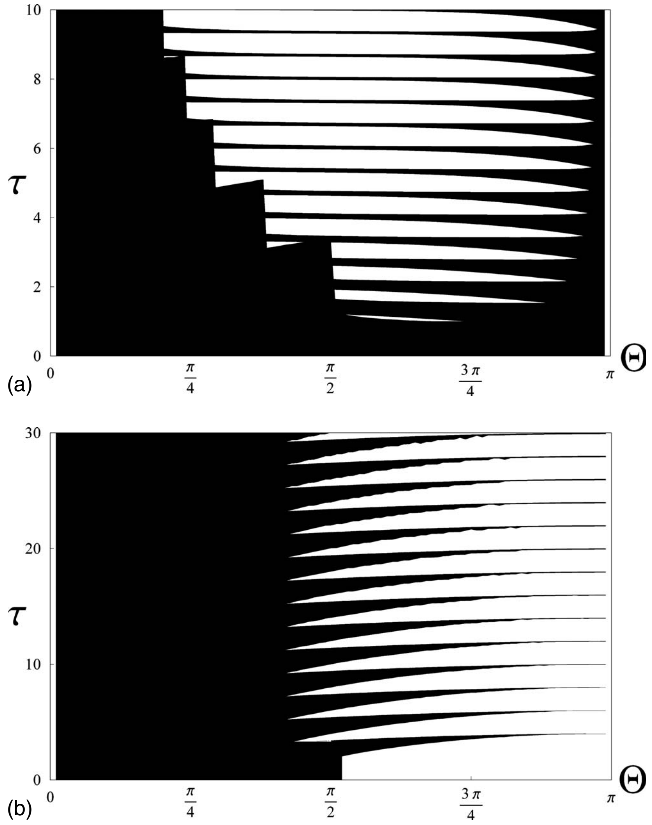

FIG. 9. (a) Region (black) of RPM parameter space $\mathcal{Q}$ which contains stable period-1 fixed points prior to period doubling, (b) the same region corresponding to fixed points after reverse period doubling.

accounted for. This rate is quantified by the infinite time Lyapunov exponent λ_∞

$$\lambda_\infty = \lim_{t\to\infty} \lambda_t = \lim_{t\to\infty}\frac{1}{t}\log|\Lambda(t)|, \tag{34}$$

where $\Lambda(t)$ is calculated as above. For globally ergodic flows, λ_∞ is unique regardless of initial position as any Lagrangian trajectory is space filling, however convergence of Eq. (34) with t is notoriously slow. Furthermore, as it is unknown whether a flow in parameter space $\mathcal{Q}$ is globally chaotic due to higher-order fixed points, we calculate an effective global Lyapunov exponent $\tilde{\lambda}$ from a series of finite time Lyapunov exponents $\lambda_{t,n}$ via

$$\tilde{\lambda} = \frac{1}{N}\prod_{n=1}^{N}\mathrm{sgn}(\lambda_{t,n})\sum_{n=1}^{N}\lambda_{t,n}, \tag{35}$$

for $t/\tau=10$ periods of the flow over a random sample of $N=1000$ initial positions. This effective Lyapunov exponent is zero if any initial position lies within an integrable region of the flow and corresponds to an average of λ_t otherwise. As such, $\tilde{\lambda}$ is indicates both global chaos and, if global, the averaged rate of expansion of the chaotic sea which closely approximates λ_∞ for $N=1000$. The distribution of $\tilde{\lambda}$ over $\mathcal{Q}$ is plotted in Fig. 10(a), where regions of $\tilde{\lambda}=0$ are evident around lines of constant τ arising from the ubiquitous existence of elliptic points at $\tau=2n/3$, $n=0,1,2,\ldots$. Note that the effective Lyapunov exponent distribution does not appear to recover the integrable regions predicted by the stability envelope in Fig. 9(b), as these are typically small and generally occur near the domain boundary and so it is unlikely that an initial point for λ_t falls within an elliptic island, highlighting the need for the period-1 point stability analysis above. The distribution of $\tilde{\lambda}$ can be combined with the stability regions in Fig. 8 to generate an overall map [Fig. 10(b)] of scalar transport enhancement in the RPM flow. These combined results indicate that the global optimum for scalar advection over $\mathcal{Q}_{\text{adv}}$ lies at roughly $\{\tau,\Theta\}\approx(1.7,5\pi/9)$, as indicated by the white circle in Fig. 10(b). A dyetrace simulation (Fig. 11) indicates that this parameter set gives rise to rapid global mixing and within a few iterations of the advective map $\mathbf{Y}$, most striations have been reduced to a thickness below the plot resolution. These results indicate that a robust global optimization of scalar advection within potential flows is possible, leading to rapid complete mixing in short times.

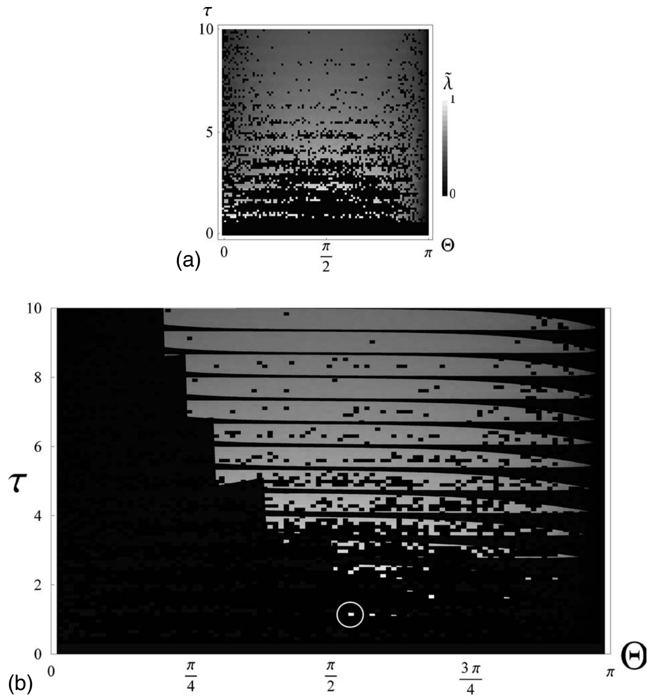

FIG. 10. (a) Distribution of effective Lyapunov exponent $\tilde{\lambda}$ over the RPM parameter space $\mathcal{Q}$, and (b) combination of period-1 stability regions and stretching results over $\mathcal{Q}$.

VI. ALTERNATE REINJECTION PROTOCOLS

For closed flows, there exist a number of different reinjection protocols such as reflected, delayed, and stochastic reinjection. Delayed reinjection corresponds to particle hold up in a finite-length pipe, stochastic reinjection corresponds to some level of fluid mixing or particle diffusion in such a pipe and reflected reinjection corresponds to a twisted pipe. In the laboratory or field setting, such effects rarely occur in

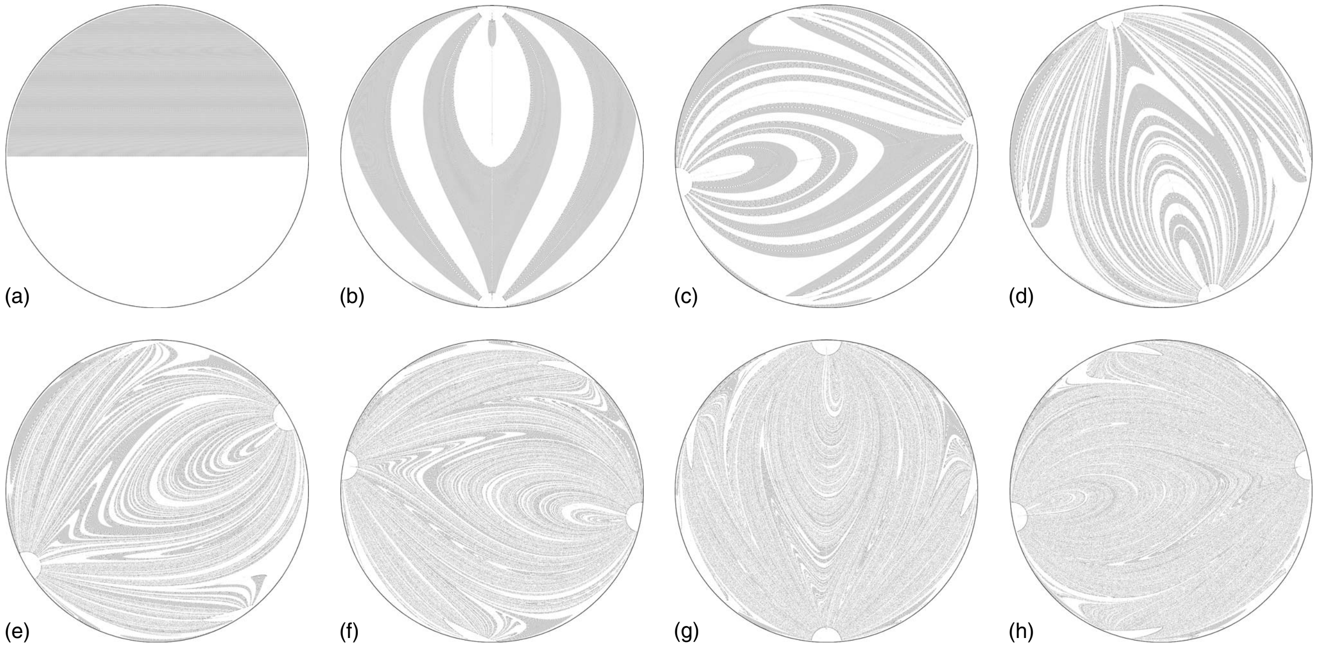

FIG. 11. Dyetrace evolution of optimal stirring protocol over $\mathcal{Q}$ at $\{\tau,\Theta\}\approx(1.7,5\pi/9)$.

isolation, however for the sake of clarity we shall briefly examine the effect of each alone upon the general transport dynamics. First, reflected reinjection involves instantaneous reinjection at the source $\mathbf{x}^{+}$ whereby the streamnumber is reversed, i.e., $\psi|_{\mathbf{x}^{+}}=-\psi|_{\mathbf{x}^{-}}$. For fixed and periodic points which undergo even numbers (including zero) of reinjections during the periodic cycle, the location, stability, and local dynamics of these points is unchanged due to the reflection symmetry Eq. (12) of the dipole flow. However, if any periodic (or fixed) point undergoes an odd number of reinjections during a cycle, then the period p cycle is replaced by a period $2p$ cycle, and the location and stability of these points may be changed. This is clearly illustrated in the Poincaré sections in Fig. 12, where the nonreflected one contains a large island on the left-hand side, and three period-3 islands on the right. In the reflected reinjection case, the elliptic island which corresponds to a nonreinjected fixed point is unchanged, whereas the period-3 cycle (which undergoes re-injection once during the cycle) is now replaced by a stable period-6 cycle, such that the original period-3 points lie between the new pairs in the period-6 cycle. However, unlike the period-doubling bifurcation, the original period-3 cycle no longer exists and these regions are in the chaotic sea. In this case the stability of the period-3 cycle is preserved, however in other cases across (τ,Θ) space, changes in stability from hyperbolic to elliptic and vice-versa are observed.

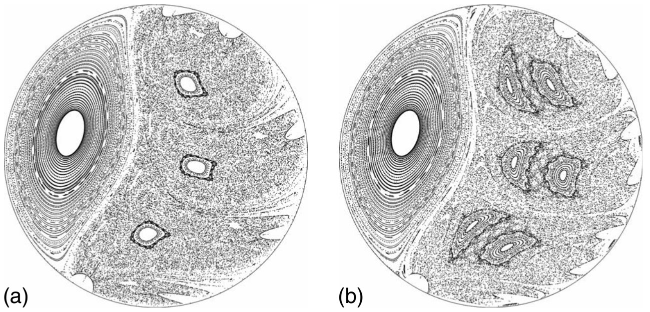

FIG. 12. Poincaré sections at $\{\tau,\Theta\}=(1/5,\pi/6)$ for (a) regular reinjection and (b) reflected reinjection.

We consider two mechanisms of stochastic reinjection; one whereby the streamnumber at $\mathbf{x}^{+}$ upon reinjection is chosen from a random uniform distribution over $[-\pi/2,\pi/2]$, and so is completely uncorrelated with ψ leaving at $\mathbf{x}^{-}$, and a second where some level of Gaussian noise (of variance σ_{ψ}^{2}) is added to the streamnumber at $\mathbf{x}^{+}$ and mapped to the domain $\psi\in[-\pi/2,\pi/2]$ by periodic boundary conditions. In both cases, the asymptotic transport dynamics are the same; any isolated regions (such as elliptic islands or isolated mixing regions) of the flow domain which do not undergo reinjection (i.e., regions which persist in the open flow case) are unchanged, whereas the remaining regions eventually mix completely due to the stochastic process at the inlet, regardless of the Lagrangian topology within this region. For random reinjection, all resonances, and hence coherent structures are destroyed upon a single reinjection event as there is no correlation between $\psi|_{\mathbf{x}^{+}}$ and $\psi|_{\mathbf{x}^{-}}$, and so mixing is rapid and ergodic. Conversely, finite perturbations via the addition of Gaussian noise result in "smearing" of coherent structures in the Lagrangian topology in a manner similar to diffusion, which asymptote with time to complete mixing. The magnitude of Gaussian noise governs the rate of convergence to the well-mixed state, as depicted in the series of finite-time Poincaré sections with increasing variance (σ_{ψ}^{2}) in Fig. 13, where persistence of the nonreinjected structure is clearly illustrated against the breakdown of the Lagrangian topology in the reinjected region. The addition of Gaussian noise to reinjection represents a dissipative operator localized around the source $\mathbf{x}^{+}$, which shares the qualitative properties of other dissipative systems, namely, contraction of phase space and possible admission of so-called "strange eigenmodes" [13] in the reinjected region.

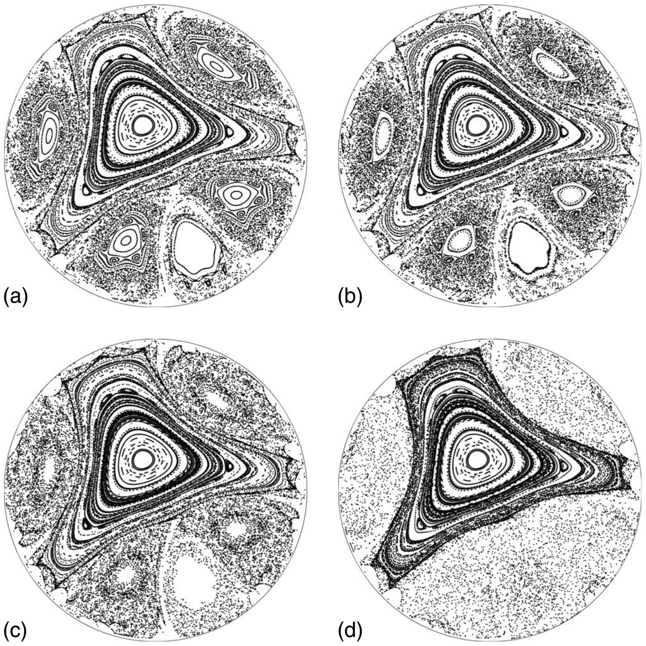

FIG. 13. Finite time Poincaré sections simulated to 1000τ at $\{\tau,\Theta\}=(1/5,3\pi/4)$ with Gaussian noise upon re-injection (a) $\sigma_{\psi}^{2}=0$ (b) $\sigma_{\psi}^{2}=10^{-6}$ (c) $\sigma_{\psi}^{2}=10^{-4}$ (d) $\sigma_{\psi}^{2}=10^{-2}$.

In the case of delayed reinjection, the domain $\mathcal{D}$ is expanded to include the finite-length pipe associated with the delay time t_d. Hold-up in the reinjection pipe does not alter the local dynamics within the flow domain, but rather transports coherent structures in the Lagrangian topology, such that an period-p point at $\{\psi,\theta\}$ which undergoes n reinjections during the period-p cycle is translated to $\{\psi,\theta-\theta_{\text{adv}}(\psi,nt_d)\}$, where values of $|\theta-\theta_{\text{adv}}(\psi,nt_d)|$ greater than $\pi/2$ correspond to fixed points which occur within the finite-length reinjection pipe. Unlike the other reinjection protocols above, the stability of these points is unchanged by the delay nt_d, and the Lagrangian topology and coherent structures undergo a small distortion due to the variance of streamline velocities with ψ. As such, the local dynamics are changed; i.e., the stable and unstable manifolds of the flow are translated to different locations and slightly stretched, but globally the transport dynamics over $\mathcal{D}$ are quantitatively similar.

VII. CONCLUSIONS

We have given a theoretical and numerical analysis of the transport properties of open and closed potential flows with respect to scalar advection, based on the RPM flow as a model system. Results from the kinematic problem suggest potential flows present no limitation to the attainment of Lagrangian chaos so long as the flow transients can be programmed to generate stretching and folding of material elements. In the limit $\tau\to 0$, the periodic reorientation creates a Hamiltonian structure that is steady and integrable, and so the breakdown of this state is necessary to the attainment of Lagrangian chaos. Symmetries in the base dipole flow of the RPM flow impart symmetry conditions on the Lagrangian topology itself and also over the flow control parameter space $\mathcal{Q}$. Base flows with different symmetries will generate different topologies. These conditions constrain the location of period-1 fixed points, which in turn govern the majority of the mixing properties of such flows. In the case of the open RPM flow, an "instability envelope" exists over which a route to chaos is achieved via a period-doubling bifurcation cascade. This envelope limits the region of parameter space $\mathcal{Q}$ which generates global chaos, where the rate of expansion along the unstable manifold is quantified by the Lyapunov exponent. Maximum stretch occurs toward the degenerate limit $\Theta\to\pi$, at which point the system collapses to a completely integrable state. The closed RPM flow is characterized by "bands of stability" in $\mathcal{Q}$ arising from stable period-1 points at $\tau=2n/3$. These stability bands exclude regions of the parameter space $\mathcal{Q}$ from the remainder which represent necessary but not sufficient conditions for the attainment of globally ergodic mixing. Transport over the remaining regions of $\mathcal{Q}$ is quantified by the effective global Lyapunov exponent which accounts for higher periodicity fixed points and identifies regions corresponding to rapid complete mixing for the closed system, as verified by dyetrace simulations. These results suggest that chaotic advection can be readily achieved within potential flows, and that the symmetries present in the base dipole flow play a significant role in programming the structure of Lagrangian topology and the mixing template.

[1] M. S. Appold and G. Garven, Econ. Geol. **95**, 1605 (2000).
[2] H. Aref, J. Fluid Mech. **143**, 1 (1984).
[3] M. Stremler and B. Cola, Phys. Fluids **18**, 011701 (2006).
[4] S. W. Jones and H. Aref, Phys. Fluids **31**, 469 (1988).
[5] J. M. Ottino, *The Kinematics of Mixing: Stretching, Chaos and Transport* (Cambridge University Press, Cambridge, 1989).
[6] J.-M. Hertzsch, R. Sturman, and S. Wiggins, Small **3**, 202 (2007).
[7] J. Evans, D. Liepmann, and A. Pisano, in Proceedings of the IEEE 10th Annual Workshop on Microelectromechanical Systems (IEEE Press, New York, 1997), pp. 96–101.
[8] G. Metcalfe, D. R. Lester, M. Trefry, and A. Ord, Proc. SPIE **6802**, 68020I (2007)
[9] H. Lamb, *Hydrodynamics*, 6th ed. (Dover, New York, 1932).
[10] G. Metcalfe, D. R. Lester, A. Ord, P. Kulkarni, M. Rudman, M. Trefry, B. Hobbs, K. Regenaur-Lieb, and J. Morris, Philisophical Transactions of the Royal Society A (to be published).
[11] G. Metcalfe, D. R. Lester, A. Ord, P. Kulkarni, M. Trefry, B. Hobbs, K. Regenaur-Lieb, and J. Morris, Philisophical Transactions of the Royal Society A (to be published).
[12] E. Ott, *Chaos in Dynamical Systems* (Cambridge University Press, Cambridge, 1993).
[13] W. Liu and G. Haller, Physica D **188**, 1 (2004).